Journal of Materials Chemistry A

PAPER

View Article Online
View Journal

Check for updates

Cite this: DOI: 10.1039/c8ta00759d

Relative stability of FeS_2 polymorphs with the random phase approximation approach

Min-Ye Zhang, Zhi-Hao Cui and Hong Jiang *

Iron disulfide (FeS_2) has attracted a lot of interest for photovoltaic and photoelectrochemical applications due to its favorable electronic and optical properties. The theoretical description of FeS_2 has been confronted with the problem of common density functional approximations failing to correctly account for the relative stability of pyrite and marcasite polymorphs of FeS_2. We address this issue by using the adiabatic-connection fluctuation-dissipation theorem (ACFDT) in the random phase approximation (RPA). The relative stability of the two polymorphs is correctly predicted, and a significantly improved agreement with experiment compared to that from local, semi-local and hybrid functionals is obtained in terms of the enthalpy of transformation, regardless of the density functional approximations used in producing the input wave functions for RPA calculations. We attribute the stability of the pyrite phase to the electron correlation related to the low energy excitation from Fe d states to the S–S σ_p^* state. Equilibrium volumes very close to the experimental values are predicted for both phases as well. The contributions of zero-point energy corrections and finite temperature effects are considered and found to be insignificant compared to dynamical correlation included in the ACFDT-RPA approach. This study highlights the importance of considering the difference in high-order dynamical correlation as described by ACFDT-RPA due to the distinction in the Kohn–Sham band structure for a correct description of the relative stability of competing phases that are energetically very close to each other.

Received 24th January 2018
Accepted 14th March 2018

DOI: 10.1039/c8ta00759d

rsc.li/materials-a

Published on 15 March 2018. Downloaded by Peking University on 01/04/2018 07:11:44.

1 Introduction

In recent decades, iron disulfide (FeS_2) has drawn considerable attention from both industrial and academic communities as a competitive candidate working material for efficient and inexpensive solar energy conversion,[1,2] mainly because of its suitable band gap (0.95 eV), extraordinary absorption coefficient, non-toxicity and low cost of raw materials. Apart from the practical synthesis of high-quality pyrite thin films for photovoltaic cells,[3,4] applications have also been explored to use FeS_2 as an electrocatalyst for photoelectrochemical cells and photo-assisted hydrogen generation.[5,6] In both natural minerals and synthesized samples, marcasite, another polymorphic phase of FeS_2, is found to coexist with pyrite.[7,8] By measuring the heat capacity of marcasite from 5 to 700 K and that of pyrite from 300 to 780 K, Grønvold and co-workers determined that marcasite is metastable with respect to pyrite, and the enthalpy of transformation at zero kelvin from marcasite to pyrite is -0.99 ± 0.05 kcal mol^{-1} [-42.9 ± 0.2 meV per formula unit (f.u.)].[9] Kinetic factors are believed to be important in the formation of marcasite.[7,10] It has been recently shown theoretically by using a quasi-thermodynamic model that the surface stability of FeS_2 nanoparticles at the nucleation stage plays an essential role in the pH-controlled phase selection in the hydrothermal synthesis.[11]

First-principles electronic structure calculations with Kohn–Sham (KS) density functional theory (DFT)[12,13] have been widely performed and provided valuable insights to understand the structural, thermodynamical and electronic properties of FeS_2.[14–20] However, highly scattered theoretical results have been reported regarding the relative stability of pyrite and marcasite.[17–19] Spagnoli *et al.* carried out DFT calculations with a range of approximate exchange-correlation (XC) functionals implemented in several packages.[17] It was shown that the local density approximation (LDA)[13] and Perdew–Burke–Ernzerhof (PBE)[21] generalized gradient approximation (GGA) predicted wrongly that marcasite is more stable than pyrite, while Sun *et al.* reported the opposite by LDA.[18] In the meanwhile, PBEsol[22] and AM05 (ref. 23) XC functionals were shown to be able to reproduce the correct stability order, but the calculated enthalpy of transformation from marcasite to pyrite was underestimated by one order of magnitude compared to experiment.[17] In addition, equilibrium volumes are underestimated significantly compared to the experimental values for both phases when LDA or PBEsol is used.[17,18] Total energy calculation of both phases with experimental lattice constants with a Heyd–Scuseria–Ernzerhof (HSE) hybrid functional[24,25]

Beijing National Laboratory for Molecular Sciences, State Key Laboratory of Rare Earth Material Chemistry and Application, Institute of Theoretical and Computational Chemistry, College of Chemistry and Molecular Engineering, Peking University, 100871 Beijing, China. E-mail: jianghchem@pku.edu.cn

Published on 15 March 2018. Downloaded by Peking University on 01/04/2018 07:11:44.

suggests a stability preference for pyrite by 5.2 meV per f.u.[18] Furthermore, to address the self-interaction error (SIE) in approximate density functionals, especially for transition metal compounds,[26] the band structure and energetics of FeS_2 polymorphs are also studied by DFT with the Hubbard-U correction (DFT + U).[17,18] Particularly, Spagnoli and coworkers showed that it is possible to reverse the stability of marcasite over pyrite predicted by PBE with a sufficiently large effective Hubbard U parameter, but other properties, such as equilibrium lattice constants, are described very badly in that case.[17]

In this work we investigate the relative stability of pyrite and marcasite by using the adiabatic-connection fluctuation-dissipation theorem (ACFDT) in the random phase approximation (RPA), which has been applied to many different systems with remarkable improvement compared to traditional density functional approximations.[27–30] Although the RPA total energy is not fully SIE free due to the complete neglect of the exchange-correlation kernel (*i.e.* the contribution from exchange-like and ladder terms in the diagrammatic expansion of correlation energy), it has proved to be a good approximation, for example, in the prediction of the cohesive energy and lattice constants of bulk solids,[31–34] the formation energy of transition metal oxides,[35] the energy difference between different polymorphs,[32,36–38] surface adsorption[39] and the interactions in low-dimensional materials, layered systems and interfaces.[40–43] Some features of RPA are believed to be responsible for its success within these diverse areas:[27,29,30] (1) despite SIE in the RPA correlation term, the exchange term is treated exactly to remove the unphysical self-interaction in the Hartree energy; (2) the nonlocal and dynamical correlation is incorporated by renormalizing the non-interacting KS response function with the Coulomb kernel, which describes the long-range van der Waals dispersion interaction seamlessly[44] as well as an accurate dynamical screening effect in the small gap systems; and (3) the RPA correlation takes partial account of static correlation, *e.g.* left–right correlation in hydrogen molecules within the spin-restricted framework,[45,46] and is a good approximation for systems with multi-configuration nature.[47,48] It is therefore of great interest to investigate the FeS_2 phase stability issue by using the ACFDT-RPA approach, as both pyrite and marcasite have a small optical band gap near 1 eV.[1,49] The correlation effect might be essential to overcome the obstacle confronted by traditional density functional approximations in evaluating the relative stability of the energetically close FeS_2 polymorphs.

The paper is organized as follows. The next section describes the basic theory and computational details employed in this study. In the third section, we present the main results, including equilibrium volumes, bulk moduli and relative total energy of the two FeS_2 phases, calculated by ACFDT-RPA and by various traditional DFAs as well for comparison. We offer a detailed discussion on the relationship between the RPA correlation energy and Kohn–Sham band structure and discuss the contribution from lattice vibrations in evaluating the relative stability of the polymorphs. In the final section we summarize the main findings with some general concluding remarks.

2 Theory and method

Total energy in the ACFDT-RPA approach

In the ACFDT framework, the expression for the total energy of the electron-nucleus system is

$$E_{\mathrm{tot}}^{\mathrm{ACFDT}} = T_{\mathrm{KS}} + E_{\mathrm{n-n}} + E_{\mathrm{e-n}} + E_{\mathrm{H}} + E_{\mathrm{x}} + E_{\mathrm{c}} \tag{1}$$

where the six terms on the right-hand side (r.h.s.) are the kinetic energy of the KS non-interacting electronic system, the electrostatic Coulomb repulsion between nuclei charges, the electron–nuclei interacting energy, the classical electronic Coulomb repulsion energy (Hartree energy), the exact exchange energy and the correlation energy, respectively. Particularly, E_{x} is the Hartree–Fock exchange energy calculated by using KS orbitals $\{\psi_i^{\mathrm{KS}}\}$, and the sum of the first five terms on the r.h.s. of eqn (1) is just the Hartree–Fock total energy evaluated with KS orbitals $\{\psi_i^{\mathrm{KS}}\}$, termed as the exact exchange (EXX) total energy henceforth.

The ACFDT correlation energy E_{c} in eqn (1) is written as

$$E_{\mathrm{c}} = -\frac{1}{2\pi}\int_0^1 \mathrm{d}\lambda \int \mathrm{d}\mathbf{r}\mathrm{d}\mathbf{r}' \frac{1}{|\mathbf{r}-\mathbf{r}'|}\int_0^\infty \mathrm{d}\omega\left[\chi^\lambda(\mathbf{r},\mathbf{r}',\mathrm{i}\omega) - \chi^0(\mathbf{r},\mathbf{r}',\mathrm{i}\omega)\right] \tag{2}$$

where $\chi^\lambda(\mathbf{r},\mathbf{r}',\mathrm{i}\omega)$ is the linear density-response function of the electronic system with λ-scaled Coulomb interaction and $\chi^0(\mathbf{r},\mathbf{r}',\mathrm{i}\omega)$ is that of the KS system. In principle, $\chi^\lambda(\mathbf{r},\mathbf{r}',\mathrm{i}\omega)$ is connected with $\chi^0(\mathbf{r},\mathbf{r}',\mathrm{i}\omega)$ by the Dyson equation

$$\chi^\lambda(\boldsymbol{r},\boldsymbol{r}',\mathrm{i}\omega) = \chi^0(\mathbf{r},\mathbf{r}',\mathrm{i}\omega) + \int \mathrm{d}\mathbf{r}_1\mathrm{d}\mathbf{r}_2\chi^0(\mathbf{r},\mathbf{r}_1,\mathrm{i}\omega)f_{\mathrm{Hxc}}^\lambda(\mathbf{r}_1,\mathbf{r}_2,\mathrm{i}\omega)\chi^\lambda(\mathbf{r}_2,\mathbf{r}',\mathrm{i}\omega) \tag{3}$$

where the so-called Hartree-exchange-correlation kernel of the λ-scaled interacting system is written as

$$f_{\mathrm{Hxc}}^\lambda(\mathbf{r}_1,\mathbf{r}_2,\omega) = \frac{\lambda}{|\mathbf{r}_1-\mathbf{r}_2|} + f_{\mathrm{xc}}^\lambda(\mathbf{r}_1,\mathbf{r}_2,\omega) \tag{4}$$

with $f_{\mathrm{xc}}(\mathbf{r}_1,\mathbf{r}_2,\omega)$ being the exchange-correlation kernel. In RPA, the non-trivial $f_{\mathrm{xc}}^\lambda(\mathbf{r}_1,\mathbf{r}_2,\omega)$ is neglected and the integration over λ in eqn (2) can be performed analytically, resulting in the RPA correlation energy

$$E_{\mathrm{c}}^{\mathrm{RPA}} = \int_0^\infty \frac{\mathrm{d}\omega}{2\pi}\mathrm{Tr}\{\ln[1-\chi^0(\mathrm{i}\omega)\mathbf{v}] + \chi^0(i\omega)\mathbf{v}\} \tag{5}$$

where $\mathbf{v}$ is the bare Coulomb interaction and Tr indicates the trace of the matrix. From a physical point of view, within RPA the electrons are approximated to respond to the total field as if they are non-interacting,[50–52] and only the ring diagrams are evaluated for the polarizability in Feynman diagrammatic analysis.[53]

In periodic systems, given the Kohn–Sham eigenfunction $\psi_{n\mathbf{k}}(\mathbf{r})$ and the corresponding eigenvalue $\varepsilon_{n\mathbf{k}}$ with the band index n and wave vector $\mathbf{k}$ in the first Brillouin zone (BZ), obtained by solving the KS equation, the response function in the reciprocal space can be expressed as[54,55]

 This journal is © The Royal Society of Chemistry 2018

Published on 15 March 2018. Downloaded by Peking University on 01/04/2018 07:11:44.

$$\chi^0_{\mathbf{G}\mathbf{G}'}(\mathbf{q},\mathrm{i}\omega) = \frac{1}{\Omega}\sum_{n,n',\mathbf{k}} 2\left(f_{n'\mathbf{k}+\mathbf{q}} - f_{n\mathbf{k}}\right)\frac{M^{\mathbf{k}*}_{nn'}(\mathbf{q},\mathbf{G}')M^{\mathbf{k}}_{nn'}(\mathbf{q},\mathbf{G})}{\varepsilon_{n'\mathbf{k}+\mathbf{q}} - \varepsilon_{n\mathbf{k}} - \mathrm{i}\omega} \quad (6)$$

where Ω is the volume of the unit cell, $f_{n\mathbf{k}}$ the occupation number and $\mathbf{G}$ the reciprocal lattice vector. The factor 2 accounts for the spin multiplicity. $M^{\mathbf{k}}_{nn'}(\mathbf{q},\mathbf{G})$ is the so-called oscillator strength[56]

$$M^{\mathbf{k}}_{nn'}(\mathbf{q},\mathbf{G}) = \langle\psi_{n\mathbf{k}}|\mathrm{e}^{-\mathrm{i}(\mathbf{q}+\mathbf{G})\cdot\mathbf{r}}|\psi_{n'\mathbf{k}+\mathbf{q}}\rangle. \quad (7)$$

In principle one may need to solve the KS equation self-consistently with a local exchange-correlation potential corresponding to $E_\mathrm{x} + E_\mathrm{c}^\mathrm{RPA}$ by solving the corresponding optimized effective potential (OEP) equation,[57] or equivalent Sham–Schlüter equation.[58,59] In this work we restrict our ACFDT-RPA calculation within a non-self-consistent scheme, using the KS orbitals and energies from a particular density functional approximation (DFA) X as the input to calculate the RPA total energy, and denote such a computational scheme as RPA@X. We check the dependence of the relative energy between pyrite and marcasite on the input KS orbital wave functions and energies by considering several different DFAs.

Phonon spectra in a finite displacement method

In many cases, lattice vibrations can also play an important role in determining the thermodynamic stability of crystal phases.[60–62] The vibrational internal energy, consisting of the zero-point energy (ZPE) and phonon excitation energy at finite temperature, can be obtained from the phonon spectrum within the harmonic approximation, which can be calculated by either using density functional perturbation theory (DFPT)[63] or the finite displacement method (FDM).[64–66] The latter is employed in the present FeS_2 study.

In the FDM approach,[66] a supercell is constructed and all possible displacements of the atoms in the primitive cell are performed to calculate forces on each atom in the supercell. The force constant matrix $\mathbf{\Phi}$ can be calculated as[66]

$$\mathbf{\Phi}_{lj\alpha,l'j'\beta} = \frac{\partial^2 E}{\partial u_{lj\alpha}\partial u_{l'j'\beta}} \approx -\frac{F_{l'j'\beta}(u_{lj\alpha})}{u_{lj\alpha}}. \quad (8)$$

where $u_{lj\alpha}$ denotes a small displacement of the j-th atom in the l-cell along the Cartesian direction α, and $F_{l'j'\beta}(u_{lj\alpha})$ the resultant force on the $l'j'$-th atom in the β direction, with all other atoms in the supercell fixed in their equilibrium positions. Taking into account the periodicity of the crystal, elements of the dynamical matrix $\boldsymbol{D}(\mathbf{q})$ are determined by

$$\boldsymbol{D}_{j\alpha;j'\beta}(\mathbf{q}) = \frac{1}{\sqrt{M_j M_{j'}}}\sum_{l'}\mathbf{\Phi}_{0j\alpha,l'j'\beta}\mathrm{e}^{\mathrm{i}\mathbf{q}\cdot\mathbf{R}_{l'}}, \quad (9)$$

where $\mathbf{q}$ denotes the phonon wave vector, and $\mathbf{R}_{l'}$ the lattice vector of the l'-th cell. The supercell has to be large enough such that neglecting the response of atoms out of the supercell, *i.e.* truncating the sum over l' in eqn (9), will not introduce significant error. The frequency $\omega_\nu(\mathbf{q})$ of the phonon mode $e_\nu(\mathbf{q})$ can be obtained by diagonalizing the dynamical matrix $\mathbf{D}(\mathbf{q})$ with

$$\mathbf{D}(\mathbf{q})e_\nu(\mathbf{q}) = \omega_\nu{}^2(\mathbf{q})\mathbf{e}_\nu(\mathbf{q}), \quad (10)$$

and the phonon dispersion relation and density of states (ph-DOS) can be obtained accordingly.

Using the phonon energy spectrum, the vibrational internal energy (U_vib) at a finite temperature T can be readily evaluated by

$$U_\mathrm{vib}(T) = \sum_{\mathbf{q},\nu}\hbar\omega_\nu(\mathbf{q})\left\{\frac{1}{2} + \frac{1}{\exp[\hbar\omega_\nu(\mathbf{q})/k_\mathrm{B}T] - 1}\right\}. \quad (11)$$

where the first term in the summation gives the zero-point energy (ZPE). At temperature T and pressure p, the enthalpy difference between two crystal phases can be written as the sum of three contributions,

$$\Delta H(T) = \Delta E_\mathrm{tot} + \Delta U_\mathrm{vib}(T) + p\Delta V \quad (12)$$

where ΔE_tot and ΔV are the difference in the ground state energy and the equilibrium volume of the unit cell between two polymorphs, respectively. For solids at low temperature and ambient pressure, the most important contribution in the second term is that of ZPE, and the $p\Delta V$ term is in the order of 10^{-2} to 10^{-1} J mol^{-1}, which is negligible in the current case.

Computational details

All calculations are performed by using DFT with the projector augmented wave (PAW) method[67] implemented in the Vienna *ab initio* Simulation Package (VASP).[68] The GW-tuned approximately norm-conserving PAW pseudopotentials (PPs) are used in all calculations,[69,70] which is important to ensure the numerical accuracy of the RPA total energy, as demonstrated in our previous study of the TiO_2 phase stability.[38] In particular, the 3s, 3p semi-core states of Fe are treated explicitly in the valence part. Several different density functional approximations, including LDA, GGA in the PBE[21] and PBEsol[22] variants, GGA + U (PBE + U, PBEsol + U), the HSE06 hybrid functional,[24,25] PBE with the D3 correction,[71] the van der Waals density functional (vdW-DF) optB88-vdW[72] and recently developed meta-GGA SCAN,[73] have been considered to investigate their performance in predicting the relative stability of FeS_2 polymorphs. For GGA + U calculations, we have adopted the Dudarev scheme[74] and the effective U parameter is set as 2.0 eV for Fe d orbitals only, as suggested in a previous study.[17] The Gaussian scheme is used for the occupation of the states near the Fermi level with a smearing width of 0.05 eV. An energy cutoff of 500 eV for the plane wave expansion of wave functions is used to optimize the crystal structures. A 6 × 6 × 6 (7 × 6 × 10) Γ-centered Monkhorst–Pack $\mathbf{k}$-mesh is employed for numerical integration over the first Brillouin zone of a pyrite (marcasite) primitive cell, corresponding to 24 (96) points in the irreducible Brillouin zone (IBZ). The electronic energy convergence criterion is 10^{-7} eV and the criterion for the force convergence is 10^{-4} eV Å^{-1} for each atom in LDA, GGA, GGA + U, PBE-D3 and optB88-vdW calculations, while 10^{-6} eV and 3×10^{-3} eV Å^{-1} are set respectively for SCAN and HSE06. To obtain the ground state energy E_0, equilibrium crystal volume V_cell and bulk modulus B_0

Published on 15 March 2018. Downloaded by Peking University on 01/04/2018 07:11:44.

of each phase within DFA X, a set of crystal structures with different volumes are optimized by fully relaxing the internal coordinates and the unit cell shape, and the energy-volume data are then fitted with the Birch–Murnaghan (BM) equation of state (EOS).[75,76] The relative total energy difference between pyrite and marcasite is defined as $\Delta E_{\mathrm{P-M}} = E_{0,\mathrm{P}} - E_{0,\mathrm{M}}$, and a negative $\Delta E_{\mathrm{P-M}}$ indicates the stability of pyrite over marcasite, provided that the contribution from lattice vibration is negligible.

For non-self-consistent ACFDT-RPA calculations, the energy cutoff for the planewave expansion is 450 eV, and the Brillouin zone sampling is the same as the structural optimization. The input wave functions for RPA calculations are generated by converging the DFT total energy within 10^{-8} eV. The wave functions calculated from LDA, PBE, PBEsol, PBE + U and HSE06 XC functionals are tested for the dependence of RPA total energy on the initial input. The frequency integration in eqn (5) is performed in the Gauss–Legendre scheme, with a 16-point frequency grid along the axis. Considering the slow convergence of the RPA correlation energy with respect to the energy cutoff for the response function, E_{cut}^{χ}, the converged E_{c} is obtained by extrapolating to infinite cutoff according to[31]

$$E_{\mathrm{c}}^{\mathrm{RPA}}\left(E_{\mathrm{cut}}^{\chi}\right) = E_{\mathrm{c}}^{\mathrm{RPA},\infty} + \frac{A}{\left(E_{\mathrm{cut}}^{\chi}\right)^{3/2}}. \quad (13)$$

where $E_{\mathrm{c}}^{\mathrm{RPA},\infty}$ is the converged value. We have tested the convergence of relative ACFDT-RPA total energy with respect to the energy cutoff and the $\mathbf{k}$ points, and the result is converged within 5 meV with current settings. Since the structure optimization with the ACFDT-RPA approach is computationally exhaustive, while possible,[77] we obtain V_{cell}, E_0 and B_0 for RPA@X by first performing ACFDT-RPA calculations for the structures with different volumes, which are optimized within the corresponding DFA X beforehand, and then fitting the energy-volume data with BM-EOS.

Phonon calculations by FDM are performed by taking advantage of the PHONOPY code[78] as an interface to VASP, within the functional approximations LDA, PBE and PBEsol. A $2 \times 2 \times 2$ supercell is constructed based on the respectively optimized structure. The calculated vibrational internal energy is added to the total energy calculated from DFA X or RPA@X to determine the enthalpy difference of two phases according to eqn (12).

3 Results and discussion

Lattice structures, bulk moduli and relative total energy

The structural difference of FeS_2 polymorphs has been intensively discussed in the literature.[79,80] The conventional unit cell of pyrite and marcasite consists of four and two FeS_2 units, respectively, as shown in Fig. 1. In the cubic pyrite cell (space group $Pa\bar{3}$), Fe atoms form a face-centered cubic lattice. The S_2 dumbbells occupy the octahedral interstitials and their bonding axes are aligned along different $\langle 111 \rangle$ crystallographic axes exclusively. The orthorhombic marcasite phase (space group $Pnnm$) can be seen as a distorted rutile structure, resulting from

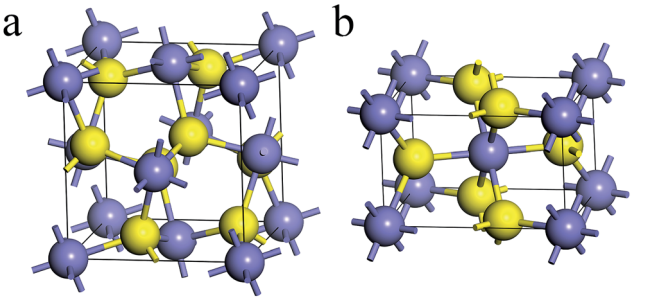

Fig. 1 Crystal structures of the two FeS_2 polymorphic phases: (a) pyrite and (b) marcasite. Yellow (blue) spheres represent S (Fe) atoms.

S–S bonding in the (001) plane.[80] The most important difference between the two phases is the way of connection of the FeS_6 octahedra: octahedra in pyrite are connected to twelve neighbours in a corner-sharing manner, while in marcasite they share corners with eight neighbours and edges with another two. Pyrite is packed more tightly than marcasite.

Table 1 shows the collection of the equilibrium volumes of the unit cell V_{cell} and bulk moduli B_0 of both FeS_2 polymorphs predicted with different approaches. DFT within PBE, HSE06 and SCAN are able to predict the volumes of both phases in good agreement with experimental values, while LDA and PBEsol underestimate V_0 significantly by about 7(6)% and 5(4)% for pyrite (marcasite), respectively. When Hubbard-U correction is included in GGA, the equilibrium volumes increase slightly, consistent with previous theoretical studies.[17,18] On the other hand, the ACFDT-RPA approach, irrespective of the density functional approximation used to generate input KS orbital wave functions and energies, predicts very accurate equilibrium volumes for both FeS_2 phases. The discrepancy between theory and experiment is slightly bigger when the hybrid functional HSE06 is used as the input, which could be related to the largely overestimated band gap for FeS_2 phases by HSE06.[18,83,84] A significant improvement is also observed for the prediction of the bulk moduli of both phases. The excellent performance of the RPA approach to describe the equilibrium structural properties of FeS_2 is consistent with previous studies of the RPA approach to many sp semiconductors and transition metals.[31–33]

Table 1 also shows the collection of the total energy difference between pyrite and marcasite per formula unit, *i.e.* $\Delta E_{\mathrm{P-M}}$, from different approaches. Among local or semi-local density functional approximations, LDA and PBEsol give the qualitatively correct prediction on the stability order, although the values of $\Delta E_{\mathrm{P-M}}$ from them are dramatically underestimated compared to the experimental enthalpy difference between pyrite and marcasite. In contrast, PBE and SCAN lead to a qualitatively wrong prediction regarding the relative stability of the two phases. It is noteworthy that the SCAN functional, the recently proposed meta-GGA that has performed remarkably well for many diversely bonded systems,[85] predicts a preference of 31.7 meV per f.u. for marcasite to pyrite, and the discrepancy from experiment is even larger than that of the PBE results. To consider the possible roles played by the long-range van der Waals (vdW) dispersion interactions in determining the FeS_2

 This journal is © The Royal Society of Chemistry 2018

Published on 15 March 2018. Downloaded by Peking University on 01/04/2018 07:11:44.

Table 1 The equilibrium volume of the unit cell V_{cell}, the bulk modulus B_0 for each polymorphic phase of FeS_2, and the relative energy ΔE_{P-M} (see the text for definition) calculated with different approaches. The enthalpy difference ΔH_{P-M} is calculated by adding zero-point energy (ZPE) to ΔE_{P-M}. Relative errors (%) of predicted V_{cell} and B_0 with respect to the referenced experimental results are indicated in parentheses. The square brackets indicate that the phonon correction calculated with PBE is used

	V_{cell} (Å^3)		B_0(GPa)		ΔE_{P-M}	ΔH_{P-M}
Method	P	M	P	M	(meV per f.u)	(meV per f.u)
LDA	148.19 (−6.7)	76.49 (−6.2)	195.6 (25.8)	184.2 (25.7)	−7.3	−5.9
PBE	157.97 (−0.5)	81.52 (0.0)	157.0 (1.0)	149.3 (1.9)	27.9	29.5
PBEsol	151.10 (−4.9)	78.02 (−4.3)	182.7 (17.5)	172.5 (17.7)	−4.5	−3.1
PBE + U	161.08 (1.4)	82.65 (−1.4)	140.0 (−10.0)	140.0 (−4.4)	28.3	
PBEsol + U	152.98 (−3.7)	78.70 (−3.4)	169.3 (8.9)	169.0 (15.4)	4.4	
HSE06	159.23 (0.3)	81.26 (−0.3)	133.8 (−14.0)	135.8 (−7.3)	−5.2	
PBE-D3	155.66 (−2.0)	80.31 (−1.5)	162.6 (4.6)	155.2 (5.9)	16.0	
optB88-vdW	160.38 (1.0)	82.69 (1.4)	153.6 (−1.2)	145.8 (−0.5)	25.5	
SCAN	159.28 (0.3)	81.49 (−0.0)	144.2 (7.3)	146.9 (0.3)	31.7	
RPA@LDA	158.88 (0.0)	82.01 (0.6)	153.3 (−1.4)	149.4 (2.0)	−30.7	−29.3
RPA@PBE	158.86 (0.0)	82.01 (0.6)	152.9 (−1.8)	149.2 (1.8)	−24.0	−22.4
RPA@PBEsol	158.75 (−0.0)	81.98 (0.6)	153.3 (−1.4)	149.2 (1.8)	−25.2	−23.8
RPA@PBE + U	158.00 (−0.5)	81.51 (0.0)	161.3 (3.7)	157.8 (7.7)	−19.1	[−17.5]
RPA@HSE06	156.27 (−1.6)	80.21 (−1.6)	162.1 (4.2)	162.0 (10.6)	−15.9	[−14.3]
Exp.	158.82[a]	81.51[a]	155.5 ± 0.2[b]	146.5[c]		−42.9 ± 0.2[d]

[a] Ref. 20. [b] Ref. 81. [c] Ref. 82. [d] Ref. 9.

phase stability, we consider two vdW-correction schemes in the DFT framework, namely PBE-D3 and optB88-vdW. However, no significant improvement is observed with the vdW correction, and the results are still qualitatively wrong. When the Hubbard-U correction is considered, the correct stability order predicted by PBEsol is even reversed, while it does not have a significant influence on the results of PBE. A qualitatively correct prediction can also be obtained by using the HSE06 hybrid functional, which, however, still exhibits a considerable quantitative discrepancy from experiment.

On the other hand, the ACFDT-RPA approach gives rather satisfactory ΔE_{P-M} results as shown in the lower part of Table 1. The negative values of ΔE_{P-M} predicted by ACFDT-RPA calculation clearly indicate that pyrite is more stable than marcasite, and quantitatively agree well with experiment. For example, RPA@PBE gives a ΔE_{P-M} of −24.0 meV per f.u., in which an exchange-correlation correction of 51.9 meV per f.u. reverses the sign of ΔE_{P-M} and corrects the stability order wrongly predicted by PBE. A more illustrative view of the correction introduced by using the RPA approach is provided in the BM-EOS obtained by PBEsol and RPA@PBEsol as shown in Fig. 2. RPA@PBEsol succeeds in reproducing experimental equilibrium volume and predicts the energy preference for pyrite comparable to the experimental value of ΔH_{P-M}, in contrast to PBEsol which underestimates both quantities significantly. It should be noted that although the values of ΔE_{P-M} do depend on the DFA used for the calculation of input KS wave functions, ACFDT-RPA removes the uncertainty about DFAs in determining the relative stability order observed in the DFT calculations and consistently stabilizes pyrite rather than marcasite. This merit has been observed in the ACFDT-RPA calculations of the anatase and rutile phases of TiO_2.[38]

It is then important to figure out the origin of the good performance of ACFDT-RPA total energy in predicting the right stability order of FeS_2 polymorphs. The correction of the RPA correlation energy term is found to be important for the determination of equilibrium volume and bulk moduli. Table 2 shows the list of the equilibrium volumes calculated by only considering the EXX total energy evaluated with LDA, PBE and PBEsol orbitals as input (denoted as EXX@X with the corresponding DFA as X) and compares them with those from X and RPA@X. In general, EXX@X gives equilibrium volume slightly smaller than experimental values (except for EXX@PBE of pyrite). It should be mentioned that from EXX@X calculations with X being GGA + U and HSE06, neither pyrite nor marcasite possesses an energy minimum within ±10% around their respective experimental volume and exhibits a tendency to dissociate. The dissociating behaviour is remedied when the RPA correlation energy is included. The RPA correlation energy

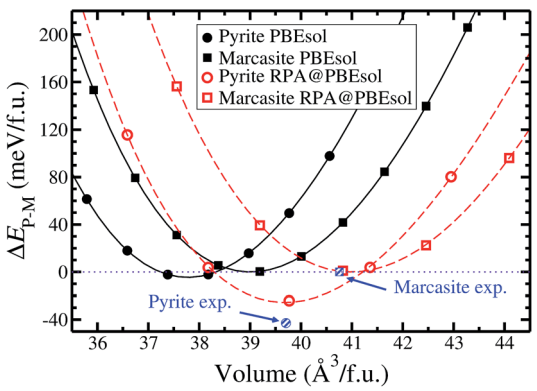

Fig. 2 Equation of state (EOS) curves of pyrite and marcasite calculated by using the PBEsol and RPA@PBEsol with the total energy of marcasite at the equilibrium volume taken as the energy zero. Experimental values are from ref. 9 and 20.

Published on 15 March 2018. Downloaded by Peking University on 01/04/2018 07:11:44.

Table 2 Equilibrium volume (Å^3) of pyrite and marcasite calculated with different methods. Errors compared to experiment (%) are shown in parentheses

	Pyrite			Marcasite		
DFA X	X	EXX@X	RPA@X	X	EXX@X	RPA@X
LDA	148.19 (−6.7)	154.3 (−2.8)	158.88 (0.0)	76.49 (−6.2)	77.0 (−5.5)	82.01 (0.6)
PBE	157.97 (−0.5)	159.1 (0.2)	158.86 (0.0)	81.52 (0.0)	78.6 (−3.6)	82.01 (0.6)
PBEsol	151.10 (−4.9)	156.2 (−1.6)	158.75 (−0.0)	78.02 (−4.3)	77.7 (−4.7)	81.98 (0.6)

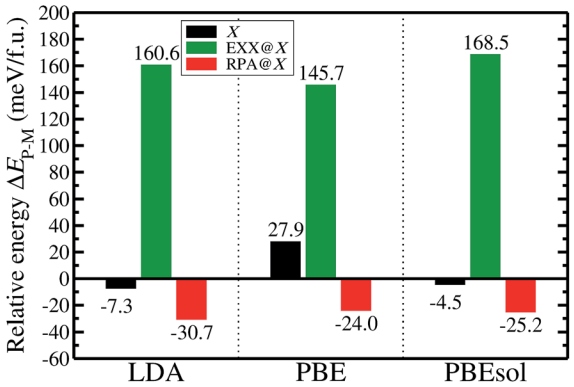

Fig. 3 Relative energy calculated by different methods: DFT within DFA X (X = LDA, PBE and PBEsol), EXX@X and RPA@X.

plays even a more crucial role in determining the relative energy of FeS_2 phases. As shown in Fig. 3, the relative energy ΔE_{P-M} calculated with EXX@X significantly stabilizes marcasite over pyrite by more than 140 meV per f.u. Including RPA correlation energy is able to remedy the qualitatively false prediction.

Electronic structure analysis of the origin of RPA correlation

Based on the observations above, the question turns to pinpointing the physical origin of the RPA correlation stabilizing pyrite over marcasite. In our previous study on the anatase and rutile phases of TiO_2,[38] we pointed out that the crystal phase (rutile) with the smaller gap would be more strongly stabilized by E_c^{RPA}. This argument was implicitly derived from the mathematical expression of E_c^{RPA}, *i.e.* eqn (5) and (6), and supported by a correlation observed between the **k**-averaged band gap $\bar{E}_g$ and the RPA correlation energy E_c^{RPA}.[38] $\bar{E}_g$ is defined as[38]

$$\overline{E}_g = \frac{1}{N_{\mathbf{k}}} \sum_{i=1}^{N_{\mathbf{k}}} (\varepsilon_{c\mathbf{k}_i} - \varepsilon_{v\mathbf{k}_i}) \quad (14)$$

where $N_{\mathbf{k}}$ is the number of **k** grids sampled in the first BZ, and c and v indicate the lowest conduction band and the highest valence band, respectively. It would be interesting to check whether a similar analysis can be used to understand the trends in FeS_2. Fig. 4(a) and (b) show the dependence of E_c^{RPA} and $\bar{E}_g$ on the unit cell volume for both FeS_2 phases calculated with the PBE XC functional. For the marcasite phase, a correlation between E_c^{RPA} and $\bar{E}_g$ can be clearly observed. For the pyrite phase, however, while $\bar{E}_g$ also decreases as the unit cell expands, similar to that in marcasite, the value of E_c^{RPA} remains almost constant, and therefore a direct correlation between $\bar{E}_g$ and E_c^{RPA} is missing. Obviously $\bar{E}_g$ as a descriptor is over-simplified. As is obvious from eqn (6), E_c^{RPA} depends not only on the splitting between occupied and unoccupied states, which can be characterized by $\bar{E}_g$, but also on the magnitude of the oscillator strength. Therefore, we suspect that a more sophisticated descriptor accounting for the band characteristics is required to build a correlation between E_c^{RPA} and the band structure in the present FeS_2 case.

To validate the necessity of explicitly considering the characteristics of wave functions in the band structure descriptor, we first analyze the differences in the electronic band structures of pyrite and marcasite in more detail. The band structure as well as the total and projected density of states near the Fermi level calculated by using the PBE XC functional are shown in Fig. 5. Both of the two phases have an indirect minimal band

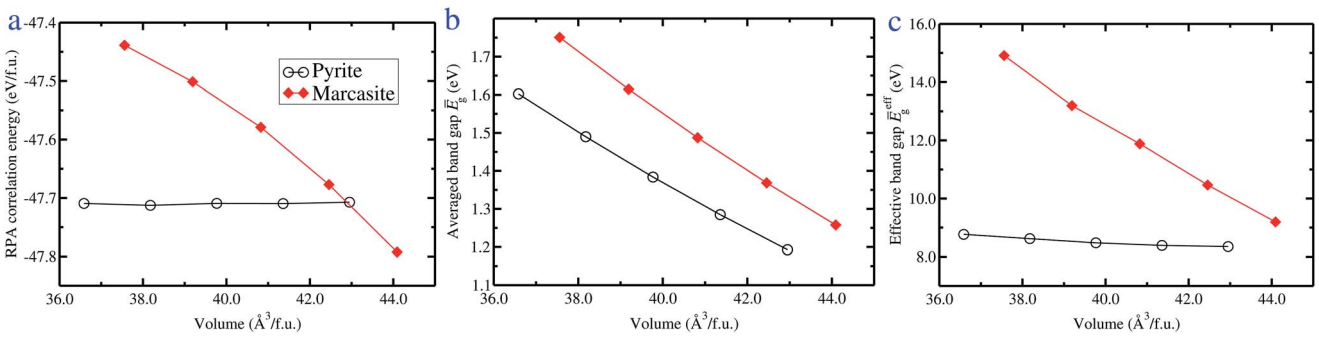

Fig. 4 Dependence of (a) RPA correlation energy, (b) band gap averaged over the Brillouin zone and (c) effective energy gap on the lattice volume of pyrite (black circle) and marcasite (red diamond), calculated by PBE.

 This journal is © The Royal Society of Chemistry 2018

Published on 15 March 2018. Downloaded by Peking University on 01/04/2018 07:11:44.

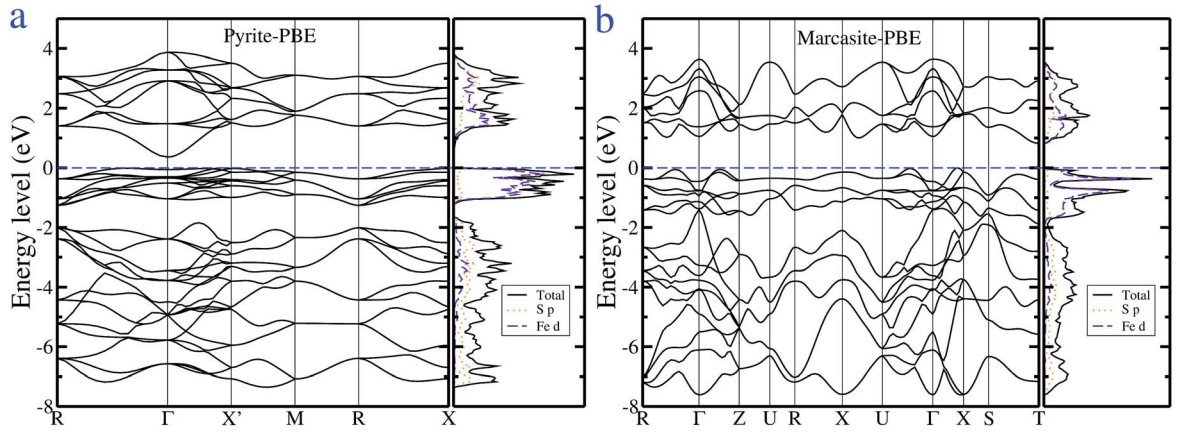

Fig. 5 Band structure and total and projected density of states of (a) pyrite and (b) marcasite at experimental volume, calculated by using the PBE functional. The energy zero has been set to the top of the valence band, indicated by the blue dashed line.

gap. The fundamental band gap of pyrite is predicted to be smaller than that of marcasite, consistent with previous studies.[18,84] Both high-lying valence band states and low-lying conduction band states are dominated by Fe-d states, but the conduction band states have significant S-p characters. In particular, the projection of Kohn–Sham orbital wave functions on the atomic orbitals reveals that in both phases the lowest conduction state at the Γ point and also the conduction band minimum (CBM) of pyrite are of S-p characters and are exclusively composed of S–S anti-bonding orbitals σ_p^*.[15] In contrast, the CBM of marcasite at the T point consists of no S-p contribution and features only Fe-d characters. In addition, the high-lying valence band states in pyrite are separated from deeper states by about 0.6 eV and show weaker dispersion compared to those in marcasite, indicating the well localized occupied 3d states (explicitly, d_{xy}, d_{xz} and d_{xz}) of Fe.

From the analysis above, we can see that the direct excitation from the high-lying valence bands to the low-lying conduction bands features dominantly d–d type transitions, except for those in the proximity of the Γ point. However, the d–d-type transitions have small oscillator strengths due to the dipole selection rule, and therefore contribute insignificantly to the RPA correlation energy, which explains why $\bar{E}_g$, which is mainly determined by the d–d transition features in FeS_2, cannot be correlated with the evolution of E_c^{RPA}. Nonetheless, it applies to the anatase and rutile phases of TiO_2 in our previous study[38] where the charge transfer excitations from O-2p to Ti-3d states are dominant. For FeS_2, the dominant contributions to E_c^{RPA} can be attributed to charge transfer-type transitions involving S-3p and Fe-3d states, which can be characterized by generalizing the **k**-averaged band gap to the following effective charge transfer gap,

$$\overline{E}_g^{eff} = \left(\frac{1}{N_{\mathbf{k}}} \sum_{i=1}^{N_{\mathbf{k}}} \frac{\left| a_{\text{S-p}}^{\mathbf{c}\mathbf{k}_i} \right|^2 \left| a_{\text{Fe-d}}^{\mathbf{v}\mathbf{k}_i} \right|^2}{\varepsilon_{\mathbf{c}\mathbf{k}_i} - \varepsilon_{\mathbf{v}\mathbf{k}_i}} \right)^{-1} \quad (15)$$

where $|a_{A\text{-}l}^{n\mathbf{k}}|^2$ is the square modulus of the projection of the Bloch state $\psi_{n\mathbf{k}}$ on the l-angular atomic orbitals of atom species A. Fig. 4(c) shows the dependence of the effective band gap $\bar{E}_g^{eff}$ on the unit cell volume for pyrite and marcasite. $\bar{E}_g^{eff}$ decreases by 0.4 eV (4%) and 5.7 eV (38%) when the volume increases from −8% to +8% of the experimental value for pyrite and marcasite, respectively. In contrast to $\bar{E}_g$, a remarkable correlation between E_c^{RPA} and $\bar{E}_g^{eff}$ can be found in both phases of FeS_2. It is therefore confirmed that the stability of pyrite over marcasite physically originates from the differences in the characters of the electronic band structures of the two phases, which can be described only in advanced (fifth-rung in Perdew's Jacob's ladder metaphor[86]) exchange-correlation functionals like RPA which depend on both occupied and unoccupied states.

To understand why the effective band gap evolves differently as a function of unit cell volume in the two FeS_2 phases, we scrutinize along a selected **k**-path in the Brillouin zone the variation of energies of states near the Fermi level as the unit cell volume changes, as shown in Fig. 6. When the volume increases from −8% to +8% of the experimental value (correspondingly band structures from black lines to red lines), the direct band gaps decrease in both phases with the exception of the region near the Γ point in pyrite. For marcasite, the narrowed effective band gap with increasing volume can be illustrated by the global decreasing of the direct band gap along the selected **k** grids. The situations are more complicated for the pyrite phase. At a small volume, the direct gap at the Γ point is much smaller than those at other **k** points and close to the fundamental gap due to the flatness of the highest valence band. With a larger volume, the gap increases near the Γ point, but decreases at other **k** points. Moreover, since the conduction band states are dominantly of Fe-d characters, but those near the Γ point are almost of S-p characters, the terms involving transitions around the Γ point in the summation of eqn (15) contribute considerably to the inverse of $\bar{E}_g^{eff}$. As a result, the reduction in these terms cancels the enlargement in the other terms to a great extent as the volume increases, and the effective band gap for pyrite is almost constant as the volume varies, in strong contrast to the situations in marcasite. We note that the unique geometrical dependence of the energy levels of conduction band states near Γ on the x parameter (equivalent to

Published on 15 March 2018. Downloaded by Peking University on 01/04/2018 07:11:44.

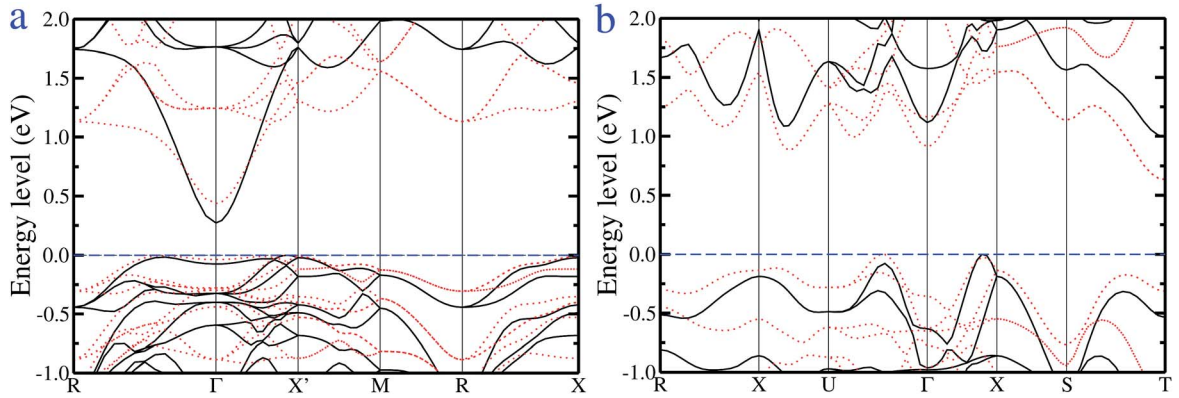

Fig. 6 Electronic band structure near the Fermi level of (a) pyrite and (b) marcasite, calculated by using the PBE functional. The black solid (red dotted) lines indicate the band dispersions of the optimized structure with 92% (108%) experimental volume. The experimental volumes are from ref. 20. The valence band maximum is aligned as the energy zero, marked by the blue dashed line.

the S–S bond length) for pyrite has been elucidated by Eyert *et al.*[15] and more recently by Kolb and Kolpak.[87] It is observed that both the S–S bond and the distance between S_2 dumbbells are lengthened when the crystal volume increases. The elongated S_2 dumbbell results in reduced hybridization between sulfur p orbitals, and subsequently a smaller $\sigma_p - \sigma_p^*$ splitting and downshift of the CBM. On the other hand, the hopping between neighbouring S_2 dumbbells is suppressed when they become more separated, leading to a weakened dispersion of S_2 σ_p^* bands and hence an upshift of the CBM. The ultimately lifted CBM is likely to be the outcome of the competition of these two contributions.

To summarize the analysis we have made, we find that the correlation between the RPA correlation energy and the band structure can be built upon the "effective band gap" descriptor concerning the direct band gap and the atomic projection of valence and conduction Bloch states. The more negative E_c^{RPA}, which leads to the stability of pyrite over marcasite at their corresponding experimental volume, can be attributed to the low-energy excitation from Fe-d to S–S σ_p^* bands based on the investigation of the geometrical dependence of the electronic band structures of the two FeS_2 phases.

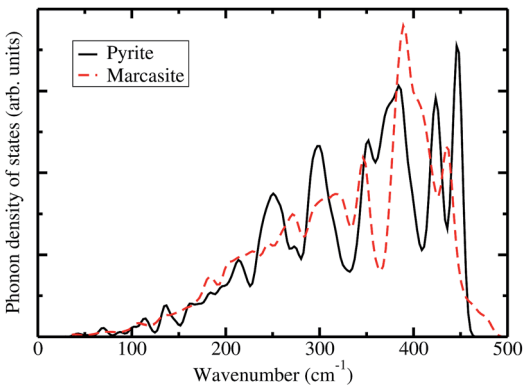

Fig. 7 Phonon density of states of pyrite and marcasite calculated by PBEsol.

Phonon contribution to the relative stability

We further investigate the contribution from lattice vibrations to the energy difference between the FeS_2 polymorphs. In Table 1, we have included into ΔE_{P-M} the ZPE correction calculated by the corresponding DFA to get the enthalpy difference ΔH_{P-M}, *i.e.* the enthalpy of transformation from marcasite to pyrite. The ZPE correction is 1.36, 1.58 and 1.44 meV per f.u. from LDA, PBE and PBEsol calculations, respectively, stabilizing marcasite regardless of the chosen functional. This agrees with the finding in a previous theoretical study.[17] The phonon density of states of each phase calculated by using PBEsol is shown in Fig. 7. Similar distribution is observed for LDA and PBE phonon calculations. Although the density distribution is similar for both phases, which illustrates the small energy difference in ZPE, the peak with the largest phonon energy at 450 cm^{-1} is observed for pyrite, and a weaker peak near 430 cm^{-1} for marcasite. This offers an explanation for the larger ZPE of pyrite. Since calculations with traditional functionals underestimate the measured thermodynamic stability of pyrite, the ZPE correction worsens the discrepancy from experiment. This

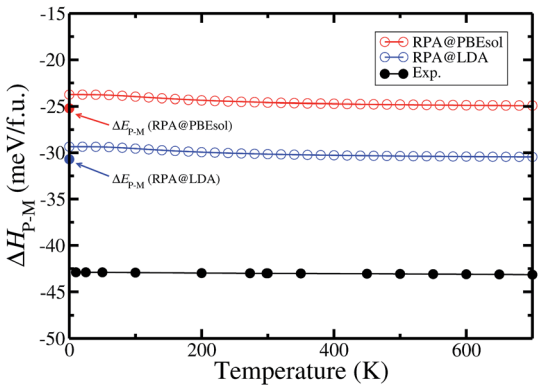

Fig. 8 Calculated and experimental enthalpy of transformation from marcasite to pyrite for a range of temperature. The experimental data are taken from ref. 9.

 This journal is © The Royal Society of Chemistry 2018

Published on 15 March 2018. Downloaded by Peking University on 01/04/2018 07:11:44.

situation is the same for RPA calculations, but the ZPE difference is small such that it brings a negligible correction and ΔH_{P-M} is almost identical to ΔE_{P-M}.

We calculate the phonon energy difference for a range of temperature and add it to ΔE_{P-M} as a correction to obtain the temperature dependence of ΔH_{P-M}. For comparison, the enthalpy of transformation from marcasite to pyrite ΔH_{P-M} measured by experiment decreases by 0.2 meV per f.u. from 0 K to 700 K.[9] In our theoretical prediction, as shown in Fig. 8, the same trend but a bigger change of 1.2 meV per f.u. is observed. It might be due to the neglect of anharmonicity in the harmonic approximation made in the phonon calculation.

4 Concluding remarks

In the present work, we have reported a systematic theoretical study on the relative stability between the pyrite and marcasite phases of FeS_2. We have reproduced the controversy found in the literature in predicting the stability order of pyrite and marcasite with different density functional approximations. We found that this issue cannot be solved by using the newly developed accurate SCAN meta-GGA, nor by considering the long-range van der Waals (vdW) interaction included in the PBE-D3 method or optB88-vdW functional. On the other hand, we found that the non-self-consistent ACFDT-RPA calculation is able to predict the correct stability order and stabilizes pyrite over marcasite, regardless of the density functional approximation used to generate the input wave functions. To bring insight from the observation, we have presented a detailed analysis on the physical origin for the success of the RPA total energy. The correlation between the RPA correlation energy and the effective charge transfer band gap suggests that not only the band gap, but also the characteristics of the Kohn–Sham states near the Fermi level have significant influences on the magnitude of the correlation energy and consequently the relative energy between the two polymorphs. This indicates that it is essential to account for the distinction in the band structure to address the relative stability of the FeS_2 polymorphs which are energetically close to each other. Accurate equilibrium volumes and bulk moduli of both FeS_2 phases have also been well reproduced by the RPA approach. Based on phonon spectra calculated by the finite-difference approach, we have also considered the contributions of the zero-point energy and finite temperature vibration excitations, which are found to be negligible to the relative stability of pyrite and marcasite.

We note that the predicted ΔH_{P-M} from the RPA total energy still shows noticeable quantitative discrepancy with experiment and is less than the experimentally measured value by about 20 meV per f.u. In recent years, there have been intensive efforts to develop new ACFDT-based methods[88–95] that go beyond the one-shot RPA approach as used in this work (see ref. 29 for a review of the latest developments). It would be highly interesting to investigate whether those new developments can further improve the quantitative agreement with experiment regarding the phase stability of the systems like TiO_2 and FeS_2. The latter can be used as a stringent test-bed to characterize the performance of newly developed advanced exchange-correlation functionals.

Conflicts of interest

There are no conflicts to declare.

Acknowledgements

This work is partly supported by the National Natural Science Foundation of China (Projects No. 21673005 and 21621061) and supported by High-performance Computing Platform of Peking University.

References

1 A. Ennaoui, S. Fiechter, C. Pettenkofer, N. Alonso-Vante, K. Büker, M. Bronold, C. Höpfner and H. Tributsch, *Sol. Energy Mater. Sol. Cells*, 1993, **29**, 289–370.
2 C. Wadia, A. P. Alivisatos and D. M. Kammen, *Environ. Sci. Technol.*, 2009, **43**, 2072–2077.
3 Y. Bi, Y. Yuan, C. L. Exstrom, S. A. Darveau and J. Huang, *Nano Lett.*, 2011, **11**, 4953–4957.
4 J. Puthussery, S. Seefeld, N. Berry, M. Gibbs and M. Law, *J. Am. Chem. Soc.*, 2011, **133**, 716–719.
5 M. Barawi, I. J. Ferrer, E. Flores, S. Yoda, J. R. Ares and C. Sánchez, *J. Phys. Chem. C*, 2016, **120**, 9547–9552.
6 Y. Xin, Z. Li, W. Wu, B. Fu and Z. Zhang, *ACS Sustainable Chem. Eng.*, 2016, **4**, 6659–6667.
7 J. B. Murowchick and H. L. Barnes, *Geochim. Cosmochim. Acta*, 1986, **50**, 2615–2629.
8 R. P. Richards, E. L. Clopton and J. A. Jaszczak, *Mineral. Rec.*, 1995, **26**, 129–138.
9 F. Grønvold and E. F. Westrum Jr, *J. Chem. Thermodyn.*, 1976, **8**, 1039–1048.
10 D. Rickard and G. W. Luther, *Chem. Rev.*, 2007, **107**, 514–562.
11 D. A. Kitchaev and G. Ceder, *Nat. Commun.*, 2016, **7**, 13799.
12 P. Hohenberg and W. Kohn, *Phys. Rev.*, 1964, **136**, B864–B871.
13 W. Kohn and L. J. Sham, *Phys. Rev.*, 1965, **140**, A1133–A1138.
14 Y. Zeng and N. A. W. Holzwarth, *Phys. Rev. B: Condens. Matter Mater. Phys.*, 1994, **50**, 8214–8220.
15 V. Eyert, K.-H. Höck, S. Fiechter and H. Tributsch, *Phys. Rev. B: Condens. Matter Mater. Phys.*, 1998, **57**, 6350–6359.
16 J. Muscat, A. Hung, S. Russo and I. Yarovsky, *Phys. Rev. B: Condens. Matter Mater. Phys.*, 2002, **65**, 054107.
17 D. Spagnoli, K. Refson, K. Wright and J. D. Gale, *Phys. Rev. B: Condens. Matter Mater. Phys.*, 2010, **81**, 094106.
18 R. Sun, M. K. Y. Chan and G. Ceder, *Phys. Rev. B: Condens. Matter Mater. Phys.*, 2011, **83**, 235311.
19 V. K. Gudelli, V. Kanchana, S. Appalakondaiah, G. Vaitheeswaran and M. C. Valsakumar, *J. Phys. Chem. C*, 2013, **117**, 21120–21131.
20 M. S. Schmøkel, L. Bjerg, S. Cenedese, M. R. V. Jørgensen, Y.-S. Chen, J. Overgaard and B. B. Iversen, *Chem. Sci.*, 2014, **5**, 1408.
21 J. P. Perdew, K. Burke and M. Ernzerhof, *Phys. Rev. Lett.*, 1996, **77**, 3865–3868.

Published on 15 March 2018. Downloaded by Peking University on 01/04/2018 07:11:44.

22 J. P. Perdew, A. Ruzsinszky, G. I. Csonka, O. A. Vydrov, G. E. Scuseria, L. A. Constantin, X. Zhou and K. Burke, *Phys. Rev. Lett.*, 2008, **100**, 136406.
23 R. Armiento and A. E. Mattsson, *Phys. Rev. B: Condens. Matter Mater. Phys.*, 2005, **72**, 085108.
24 J. Heyd, G. E. Scuseria and M. Ernzerhof, *J. Chem. Phys.*, 2003, **118**, 8207–8215.
25 J. Heyd, G. E. Scuseria and M. Ernzerhof, *J. Chem. Phys.*, 2006, **124**, 219906.
26 L. Wang, T. Maxisch and G. Ceder, *Phys. Rev. B: Condens. Matter Mater. Phys.*, 2006, **73**, 195107.
27 X. Ren, P. Rinke, C. Joas and M. Scheffler, *J. Mater. Sci.*, 2012, **47**, 7447–7471.
28 M. Casadei, X. Ren, P. Rinke, A. Rubio and M. Scheffler, *Phys. Rev. Lett.*, 2012, **109**, 146402.
29 G. P. Chen, V. K. Voora, M. M. Agee, S. Balasubramani and F. Furche, *Annu. Rev. Phys. Chem.*, 2017, **68**, 19.1–19.25.
30 A. Heßelmann, Intermolecular Interaction Energies from Kohn-Sham Random Phase Approximation Correlation Methods, in *Non-covalent Interactions in Quantum Chemistry and Physics: Theory an and Applications*, ed. A. O. de la Roza and G. A. DiLabio, Elsevier, 2017, pp. 65–136.
31 J. Harl and G. Kresse, *Phys. Rev. B: Condens. Matter Mater. Phys.*, 2008, **77**, 045136.
32 J. Harl and G. Kresse, *Phys. Rev. Lett.*, 2009, **103**, 056401.
33 J. Harl, L. Schimka and G. Kresse, *Phys. Rev. B: Condens. Matter Mater. Phys.*, 2010, **81**, 115126.
34 L. Schimka, R. Gaudoin, J. Klimeš, M. Marsman and G. Kresse, *Phys. Rev. B: Condens. Matter Mater. Phys.*, 2013, **87**, 214102.
35 J. Yan and J. K. Nørskov, *Phys. Rev. B: Condens. Matter Mater. Phys.*, 2013, **88**, 245304.
36 H. Peng and S. Lany, *Phys. Rev. B: Condens. Matter Mater. Phys.*, 2013, **87**, 174113.
37 C. E. Patrick and K. S. Thygesen, *Phys. Rev. B: Condens. Matter Mater. Phys.*, 2016, **93**, 035133.
38 Z.-H. Cui, F. Wu and H. Jiang, *Phys. Chem. Chem. Phys.*, 2016, **18**, 29914–29922.
39 X. Ren, P. Rinke and M. Scheffler, *Phys. Rev. B: Condens. Matter Mater. Phys.*, 2009, **80**, 045402.
40 A. Qaiumzadeh and R. Asgari, *Phys. Rev. B: Condens. Matter Mater. Phys.*, 2009, **79**, 075414.
41 A. Marini, P. García-González and A. Rubio, *Phys. Rev. Lett.*, 2006, **96**, 136404.
42 S. Lebègue, J. Harl, T. Gould, J. G. Ángyán, G. Kresse and J. F. Dobson, *Phys. Rev. Lett.*, 2010, **105**, 196401.
43 T. Olsen and K. S. Thygesen, *Phys. Rev. B: Condens. Matter Mater. Phys.*, 2013, **87**, 075111.
44 J. F. Dobson and J. Wang, *Phys. Rev. Lett.*, 1999, **82**, 2123–2126.
45 M. Fuchs, Y.-M. Niquet, X. Gonze and K. Burke, *J. Chem. Phys.*, 2005, **122**, 094116.
46 T. M. Henderson and G. E. Scuseria, *Mol. Phys.*, 2010, **108**, 2511–2517.
47 A. Heßelmann and A. Görling, *Phys. Rev. Lett.*, 2011, **106**, 093001.
48 F. Caruso, D. R. Rohr, M. Hellgren, X. Ren, P. Rinke, A. Rubio and M. Scheffler, *Phys. Rev. Lett.*, 2013, **110**, 146403.
49 C. Sánchez, E. Flores, M. Barawi, J. Clamagirand, J. Ares and I. Ferrer, *Solid State Commun.*, 2016, **230**, 20–24.
50 F. Aryasetiawan and O. Gunnarsson, *Rep. Prog. Phys.*, 1998, **61**, 237.
51 D. Pines and D. Bohm, *Phys. Rev.*, 1952, **85**, 338–353.
52 D. Bohm and D. Pines, *Phys. Rev.*, 1953, **92**, 609–625.
53 A. L. Fetter and J. D. Walecka, *Quantum Theory of Many-Particle Systems*, Dover Publications, New York, NY, 2003.
54 S. L. Adler, *Phys. Rev.*, 1962, **126**, 413–420.
55 N. Wiser, *Phys. Rev.*, 1963, **129**, 62–69.
56 M. Govoni and G. Galli, *J. Chem. Theory Comput.*, 2015, **11**, 2680–2696.
57 S. Kümmel and L. Kronik, *Rev. Mod. Phys.*, 2008, **80**, 3.
58 L. J. Sham and M. Schlüter, *Phys. Rev. Lett.*, 1983, **51**, 1888–1891.
59 R. W. Godby, M. Schlüter and L. J. Sham, *Phys. Rev. B: Condens. Matter Mater. Phys.*, 1988, **37**, 10159.
60 V. Ozoliņš, C. Wolverton and A. Zunger, *Phys. Rev. B: Condens. Matter Mater. Phys.*, 1998, **58**, R5897–R5900.
61 A. Y. Liu, A. A. Quong, J. K. Freericks, E. J. Nicol and E. C. Jones, *Phys. Rev. B: Condens. Matter Mater. Phys.*, 1999, **59**, 4028.
62 N. Shulumba, B. Alling, O. Hellman, E. Mozafari, P. Steneteg, M. Odén and I. A. Abrikosov, *Phys. Rev. B: Condens. Matter Mater. Phys.*, 2014, **89**, 174108.
63 S. Baroni, S. De Gironcoli, A. Dal Corso and P. Giannozzi, *Rev. Mod. Phys.*, 2001, **73**, 515.
64 G. Kresse, J. Furthmüller and J. Hafner, *Europhys. Lett.*, 1995, **32**, 729.
65 K. Parlinski, Z. Q. Li and Y. Kawazoe, *Phys. Rev. Lett.*, 1997, **78**, 4063–4066.
66 D. Alfè, *Comput. Phys. Commun.*, 2009, **180**, 2622–2633.
67 P. E. Blöchl, *Phys. Rev. B: Condens. Matter Mater. Phys.*, 1994, **50**, 17953–17979.
68 G. Kresse and J. Furthmüller, *Phys. Rev. B: Condens. Matter Mater. Phys.*, 1996, **54**, 11169–11186.
69 Y. Hinuma, A. Grüneis, G. Kresse and F. Oba, *Phys. Rev. B: Condens. Matter Mater. Phys.*, 2014, **90**, 155405.
70 A. Grüneis, G. Kresse, Y. Hinuma and F. Oba, *Phys. Rev. Lett.*, 2014, **112**, 096401.
71 S. Grimme, J. Antony, S. Ehrlich and H. Krieg, *J. Chem. Phys.*, 2010, **132**, 154104.
72 J. Klimeš, D. R. Bowler and A. Michaelides, *Phys. Rev. B: Condens. Matter Mater. Phys.*, 2011, **83**, 195131.
73 J. Sun, A. Ruzsinszky and J. Perdew, *Phys. Rev. Lett.*, 2015, **115**, 036402.
74 S. L. Dudarev, G. A. Botton, S. Y. Savrasov, C. J. Humphreys and A. P. Sutton, *Phys. Rev. B: Condens. Matter Mater. Phys.*, 1998, **57**, 1505–1509.
75 F. D. Murnaghan, *Proc. Natl. Acad. Sci. U. S. A.*, 1944, **30**, 244–247.
76 F. Birch, *Phys. Rev.*, 1947, **71**, 809–824.
77 B. Ramberger, T. Schäfer and G. Kresse, *Phys. Rev. Lett.*, 2017, **118**, 106403.
78 A. Togo and I. Tanaka, *Scr. Mater.*, 2015, **108**, 1–5.

 This journal is © The Royal Society of Chemistry 2018

Published on 15 March 2018. Downloaded by Peking University on 01/04/2018 07:11:44.

79 J. B. Goodenough, *J. Solid State Chem.*, 1972, **5**, 144–152.
80 B. Hyde and M. Okeeffe, *Aust. J. Chem.*, 1996, **49**, 867–872.
81 N. Benbattouche, G. A. Saunders, E. F. Lambson and W. Honle, *J. Phys. D: Appl. Phys.*, 1989, **22**, 670.
82 T. Chattopadhyay and H. G. von Schnering, *J. Phys. Chem. Solids*, 1985, **46**, 113–116.
83 S. G. Choi, J. Hu, L. S. Abdallah, M. Limpinsel, Y. N. Zhang, S. Zollner, R. Q. Wu and M. Law, *Phys. Rev. B: Condens. Matter Mater. Phys.*, 2012, **86**, 115207.
84 T. Schena, G. Bihlmayer and S. Blügel, *Phys. Rev. B: Condens. Matter Mater. Phys.*, 2013, **88**, 235203.
85 J. Sun, R. C. Remsing, Y. Zhang, Z. Sun, A. Ruzsinszky, H. Peng, Z. Yang, A. Paul, U. Waghmare, X. Wu, M. L. Klein and J. P. Perdew, *Nat. Chem.*, 2016, **8**, 831–836.
86 J. P. Perdew and K. Schmidt, *AIP Conf. Proc.*, 2001, **577**, 1.
87 B. Kolb and A. M. Kolpak, *Phys. Rev. B: Condens. Matter Mater. Phys.*, 2013, **88**, 235208.
88 A. Grüneis, M. Marsman, J. Harl, L. Schimka and G. Kresse, *J. Chem. Phys.*, 2009, **131**, 154115.
89 T. Olsen and K. S. Thygesen, *Phys. Rev. B: Condens. Matter Mater. Phys.*, 2012, **86**, 081103(R).
90 H. van Aggelen, Y. Yang and W. Yang, *Phys. Rev. A: At., Mol., Opt. Phys.*, 2013, **88**, 03050(R).
91 N. L. Nguyen, N. Colonna and S. de Gironcoli, *Phys. Rev. B: Condens. Matter Mater. Phys.*, 2014, **90**, 045138.
92 N. Colonna, M. Hellgren and S. de Gironcoli, *Phys. Rev. B: Condens. Matter Mater. Phys.*, 2014, **90**, 125150.
93 T. S. Jauho, T. Olsen, T. Bligaard and K. S. Thygesen, *Phys. Rev. B: Condens. Matter Mater. Phys.*, 2015, **92**, 115140.
94 J. Erhard, P. Bleiziffer and A. Görling, *Phys. Rev. Lett.*, 2016, **117**, 143002.
95 B. Mussard, D. Rocca, G. Jansen and J. G. Ángyán, *J. Chem. Theory Comput.*, 2016, **12**, 2191–2202.